Scientific Final Report for DE-FG02-04ER63870, Project 1541121

Improved Transport Processes for CCSM

PI Henry Tufo

1 A High-Order Method Modeling Environment (HOMME)

In atmospheric modeling, global spectral methods have dominated weather and climate simulation for the past two decades. However, global methods based upon the spherical harmonic basis functions require expensive non-local communication and thus have difficulty in exploiting the full potential of current high-performance parallel computers.

The primary objective of HOMME ((11)) is the development of a class of high-order scalable conservative atmospheric models for climate and general atmospheric modeling applications. The spatial discretizations are based on continuous Galerkin (spectral element method) and discontinuous Galerkin (DG). These are local methods based on high-order accurate spectral basis functions which have been shown to perform well on massively parallel supercomputers at any resolution (18). HOMME employs a cubed-sphere geometry (26) exhibiting none of the singularities present in conventional latitude-longitude spherical geometries. The element based formulation enables the use of general curvilinear geometries and adaptive conforming or non-conforming meshes.

For the HOMME grid system, a sphere is decomposed into six identical regions by an equiangular projection of the faces of an inscribed cube (21) as shown in Fig. 1. This results in a nonorthogonal curvilinear (x^1, x^2) coordinate system of central angles without singularity, for each face of the cubed-sphere, such that $x^1, x^2 \in [-\pi/4, \pi/4]$. Each face of the cubed-sphere is partitioned into $N_e \times N_e$ rectangular non-overlapping spectral elements (total $6N_e^2$). Figure 1 shows a cubed-sphere with 96 elements (the red lines indicate the edges of the cube face and blue lines are boundaries of the elements) spanning its surface, and the logical orientation of the cube faces in the computational domain. The associated metric tensor in terms of

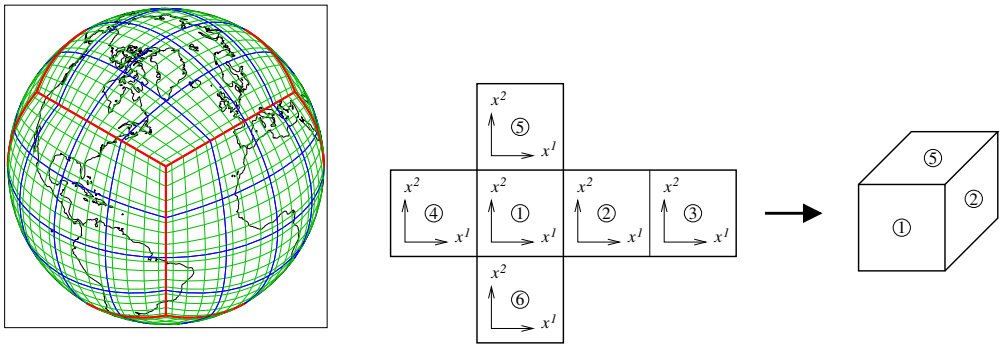

Figure 1: *Left panel shows a cubed-sphere with 96 elements ($N_e = 4$) spanning the surface of the sphere. Right panel shows the logical orientation of the cube faces (panels) and the local (x^1, x^2) coordinate system.*

longitude-latitude (λ, θ) of a sphere with radius a is given by

$$G_{ij} = A^T A; \quad A = \begin{bmatrix} a\cos\theta\,\partial\lambda/\partial x^1 & a\cos\theta\,\partial\lambda/\partial x^2 \\ a\,\partial\theta/\partial x^1 & a\,\partial\theta/\partial x^2 \end{bmatrix}.$$

The matrix A is used for transforming spherical (physical) velocity (u, v) to the covariant (u_1, u_2) and contravariant (u^1, u^2) "cubed-sphere" velocity such that

$$\begin{bmatrix} u \\ v \end{bmatrix} = A \begin{bmatrix} u^1 \\ u^2 \end{bmatrix}; \quad u^i = G^{ij}u_j,\ u_i = G_{ij}u^j,\ G^{ij} = (G_{ij})^{-1} \quad \text{and} \quad G = \det(G_{ij}).$$

1.1 Hydrostatic primitive equation in HOMME model

HOMME is currently capable of solving the hydrostatic primitive equations with spectral element and inherently conservative discontinuous Galerkin methods (21; 22; 5; 6). It has various time-stepping options combined with efficient solver technology (32; 33; 34). In addition the previous mentioned features, HOMME provides the ability to combine the continuous Galerkin (CG) and DG methods. Conservation equations are solved using the DG approach while the semi-implicit or OIFS time integration scheme is provided by the existing spectral element solvers. Preliminary simulations with Emanuel and experimental CRCP physics are promising. Integration with CAM physics is under development. Parallel performance results with idealized physics has been shown to scale on 32,768 processors of a BG/L system (30).

Efficient climate integration rates in climate modeling are paramount. For the spectral element method, combining semi-implicit time stepping and with modern preconditioning techniques yields the expected factor of three acceleration with respect to explicit time integration ((31)). Nevertheless, it still remains an open research question whether it is possible to achieve viable integration rates using a discontinuous Galerkin high-order method in combination with either explicit or semi-implicit integrators.

Most of the existing dynamical cores of atmospheric general circulation models employ a non-conservative advective form of the hydrostatic primitive equations in spherical geometry. Typically, $\sigma = p/p_s$ or hybrid pressure $\eta(p, p_s)$ coordinates are implemented in the vertical direction, where p is pressure and p_s is the surface pressure. For example, the NCAR Community Atmospheric Model (CAM) employs a hybrid coordinate, implicitly defined by the relation $p(\eta, p_s) = A(\eta)p_0 + B(\eta)p_s$ where p_0 is a constant reference pressure. The hydrostatic primitive equations consisting of the momentum, thermodynamic, mass continuity and moisture transport equations are

$$\frac{d\mathbf{v}}{dt} + f\,\hat{\mathbf{k}} \times \mathbf{v} + \nabla\Phi + R\,T_v\,\nabla \ln p = F_{\mathbf{v}} \tag{1}$$

$$\frac{dT}{dt} - \frac{R}{c_p^*}\,T_v\,\frac{\omega}{p} = Q \tag{2}$$

$$\frac{\partial}{\partial t}\left(\frac{\partial p}{\partial \eta}\right) + \nabla\cdot\left(\mathbf{v}\,\frac{\partial p}{\partial \eta}\right) + \frac{\partial}{\partial \eta}\left(\dot\eta\,\frac{\partial p}{\partial \eta}\right) = 0 \tag{3}$$

$$\frac{dq}{dt} = 0 \tag{4}$$

where $\mathbf{v}$ is the horizontal velocity, f is the Coriolis parameter, $\Phi = gh$ is the geopotential height with g the earth's mean gravitational acceleration, h the height above mean sea level, and q is the specific humidity (mixing ratio). T is the temperature and $T_v = [1 + (R/R_v - 1)q]T$ is the virtual temperature. R and R_v are gas constants. $c_p^* = [1 + (c_{p_v}/c_p - 1)q]c_p$, where c_p and c_{p_v} are the specific heat at constant pressure for dry air and water vapor, respectively. $\omega = dp/dt$ is the pressure vertical velocity, $\dot\eta = d\eta/dt$. $F_{\mathbf{v}}$ represents the momentum forcing and Q is the net heating rate from physical parameterizations. The geopotential $\Phi = gh$ is determined by the hydrostatic equation

$$\frac{\partial\Phi}{\partial\eta} = -\frac{RT_v}{p}\,\frac{\partial p}{\partial\eta}. \tag{5}$$

The material derivative appearing above is given by

$$\frac{d}{dt} = \frac{\partial}{\partial t} + \mathbf{v}\cdot\nabla + \dot\eta\,\frac{\partial}{\partial\eta}$$

Analogous to the shallow water equations, the momentum equation can be expressed in the conservative form,

$$\frac{\partial \mathbf{v}}{\partial t} + (f+\zeta)\,\hat{\mathbf{k}} \times \mathbf{v} + \dot{\eta}\frac{\partial \mathbf{v}}{\partial \eta} + \nabla E + RT_v \nabla \ln p = 0. \tag{6}$$

The flux form of the continuity, thermodynamic and tracer transport equations are generalized by,

$$\frac{\partial}{\partial t}\left(\frac{\partial p}{\partial \eta}\psi\right) + \nabla \cdot \left(\mathbf{v}\frac{\partial p}{\partial \eta}\psi\right) + \frac{\partial}{\partial \eta}\left(\dot{\eta}\frac{\partial p}{\partial \eta}\psi\right) = 0, \tag{7}$$

where ψ is a scalar field representing the potential temperature Θ or the mixing ratio q. When $\psi = 1$, the above equation is the continuity equation. In our hybrid DG/CG formulation, the conservation equations are solved using DG methods. DG discretization is applied directly to the above conservative form and maintains discrete mass conservation by design.

1.2 A Conservative Baroclinic DG Model in HOMME

Conservation of integral invariants such as mass and total energy is of fundamental importance in climate modeling. A major disadvantage of the spectral-element (SE) or classical spectral transform method based atmospheric model is that it is not inherently conservative. Another disadvantage is the vertical discretization performed by a low-order finite difference scheme which is considered to be a weak point, especially when combined with a high-order horizontal discretization. In practice, conservation is retained in such models by employing mass/energy fixers, and which is considered to be an arbitrary process (**?**). The hybrid approach by combining SE and DG methods is an option for developing a mass-conservative model, however, total energy conservation is not obvious in this approach. Therefore, it is desirable to formulate the basic equations based on hyperbolic conservation laws.

In order to address these issues, the DG shallow water model in the HOMME framework (22; 5) has been recently extended to a baroclinic model by Nair and Tufo (20). Main features of this baroclinic model are the vertical discretization and the prognostic equations which are based on hyperbolic conservation laws. The primitive equations (1)-(4) can be recast in a conservative form. The vertical discretization relies on the one-dimensional vertical Lagrangian coordinates (29) based on an "evolve and remap" approach (16). A terrain-following Lagrangian vertical coordinate can be constructed by treating any reference Eulerian coordinate such as the σ or η as a material surface.

The Lagrangian surface are subject to deform in the vertical direction during the integration, and need to be re-mapped onto a reference coordinate at regular intervals of time (Lin (16)). By virtue of this approach, the hydrostatic atmosphere is vertically subdivided into a finite number of pressure intervals or pressure *thicknesses*. Moreover, the vertical coordinates and advection terms are absent from the continuous equations (6,7). The entire 3D system can be treated as a vertically stacked shallow water DG (2D) models, where the vertical levels are coupled only by the discretized hydrostatic relation. The prognostic variables are pressure thickness δp, covariant wind vectors (u_1, u_2), potential temperature Θ, moisture variable q. In the curvilinear coordinates, the system of prognostic equations based on hyperbolic conservation laws (flux form) can be written as,

$$\frac{\partial u_1}{\partial t} + \nabla_c \cdot \mathbf{E_1} = \sqrt{G}u^2\,(f+\zeta) - RT\frac{\partial}{\partial x^1}(\ln p) \tag{8}$$

$$\frac{\partial u_2}{\partial t} + \nabla_c \cdot \mathbf{E_2} = -\sqrt{G}u^1\,(f+\zeta) - RT\frac{\partial}{\partial x^2}(\ln p) \tag{9}$$

$$\frac{\partial}{\partial t}(\Delta p) + \nabla_c \cdot \left(\mathbf{U}^i\,\Delta p\right) = 0 \tag{10}$$

$$\frac{\partial}{\partial t}(\Theta \Delta p) + \nabla_c \cdot \left(\mathbf{U}^i\,\Theta\,\Delta p\right) = 0 \tag{11}$$

$$\frac{\partial}{\partial t}(q\,\Delta p) + \nabla_c \cdot \left(\mathbf{U}^i\,q\,\Delta p\right) = 0 \tag{12}$$

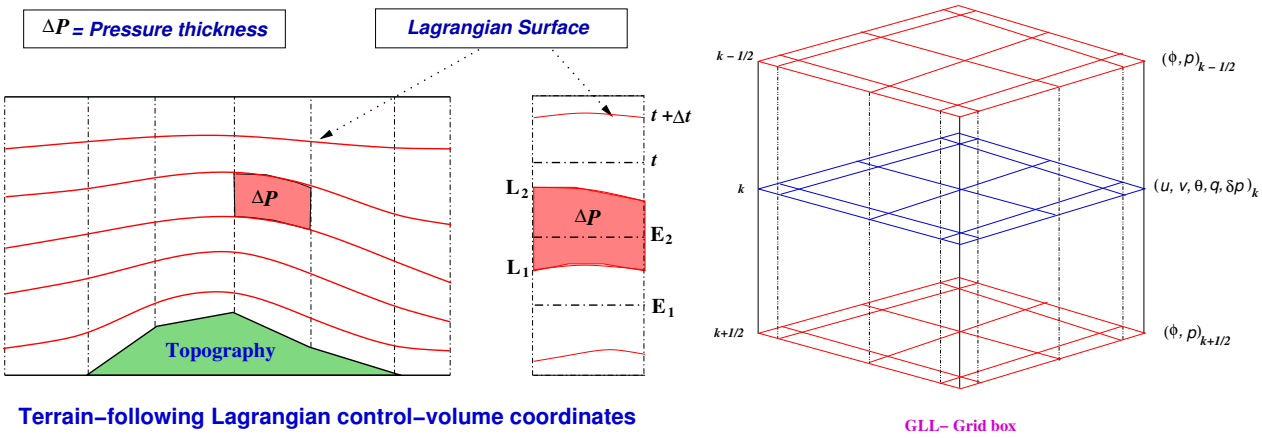

Figure 2: *Left panel shows a schematic of vertical Lagrangian coordinate. Right panel shows the 3D grid structure for the baroclinic model. During the time integration, the vertically deformed Lagrangian surfaces* (L_1L_2) *need to remapped on to a reference Eulerian frame* (E_1E_2) *at a regular interval of time.*

where

$$\nabla_c \equiv \left(\frac{\partial}{\partial x^1}, \frac{\partial}{\partial x^2}\right), \quad \mathbf{E}_1 = (E, 0), \mathbf{E}_2 = (0, E), \quad E = \Phi + \frac{1}{2}\left(u_1 u^1 + u_2 u^2\right)$$

E is the energy term, ζ is the relative vorticity. $\Phi = gh$ the geopotential height and f is the Coriolis parameter, $\Delta p = \sqrt{G}\delta p$ and $\mathbf{U}^i = \left(u^1, u^2\right)$.

Equations (8-9) are momentum equations and the mass continuity equation is (10). Note that the potential temperature Θ is advected with the mass field, and the moisture continuity equation is given by Eq.(12). For atmospheric chemistry application, more tracer transport equations can be added to the system similar to Eq. (12).

Following Lin (16), at every time step δp is predicted at model levels (see, Fig. 2) and used to determine pressure at vertical interfaces (Lagrangian surfaces) by summing the pressure thickness from top (p_{top}) to bottom (p_s), $p_\ell = p_{top} + \sum_{k=1}^{\ell} \delta p_k$. The geopotential height at interfaces is obtained by using the hydrostatic relation $(\Delta\Phi = -C_p\Theta\,\Delta\Pi)$ and summing the geopotential from bottom (Φ_s) to top, $\Phi_\ell = \Phi_s + \sum_{k=N}^{\ell} \Delta\Phi_k$. The Lagrangian surfaces deforms in the vertical direction over time, and needs to be re-mapped to a reference Eulerian coordinate in a conservative manner. We employ the 1D vertical remapping with the inherently conservative cell-integrated semi-Lagrangian (CISL) approach of Nair and Machenhauer ((23)), based on a monotonic piecewise parabolic method. The prognostic variables, u_1, u_2, q and the total energy Γ_E are conservatively re-mapped onto the Eulerian reference coordinate and Θ is extracted from Γ_E using a procedure described in (16).

1.3 The DG formulation

For simplicity, we proceed with a scalar component of the system (8)-(12):

$$\frac{\partial U}{\partial t} + \nabla \cdot \mathbf{F}(\mathbf{U}) = \mathbf{S}(\mathbf{U}), \quad \text{in} \quad \mathcal{D} \times (\mathbf{0}, \mathbf{T}), \tag{13}$$

for all $(x^1, x^2) \in \mathcal{D}$ with initial condition $U_0(x^1, x^2) = U(x^1, x^2, t = 0)$. In (13), $\mathbf{F} = (\mathbf{F_1}, \mathbf{F_2})$ is the flux function, $U = U(x^1, x^2, t)$. The computational domain $\mathcal{D}$ is the surface of the cubed-sphere, spanning six identical non-overlapping subdomains (faces) such that $\mathcal{D} = \bigcup_{\nu=1}^{6} \Omega^\nu$. Therefore, it is only necessary to consider the discretization for a single subdomain Ω as the procedure can be analogously extended to the remaining subdomains. Consider a subdomain Ω which is partitioned into $N_e \times N_e$ rectangular non-overlapping elements Ω_{ij}; $i, j = 1, 2, \ldots, N_e$, such that

$$\Omega_{ij} = \{(x^1, x^2) \,|\, x^1 \in [x^1_{i-1/2}, x^1_{i+1/2}], \quad x^2 \in [x^2_{j-1/2}, x^2_{j+1/2}]\}.$$

Thus, the total number of elements on the cubed-sphere is $M = 6 \times N_e^2$ (see Fig. 3) .

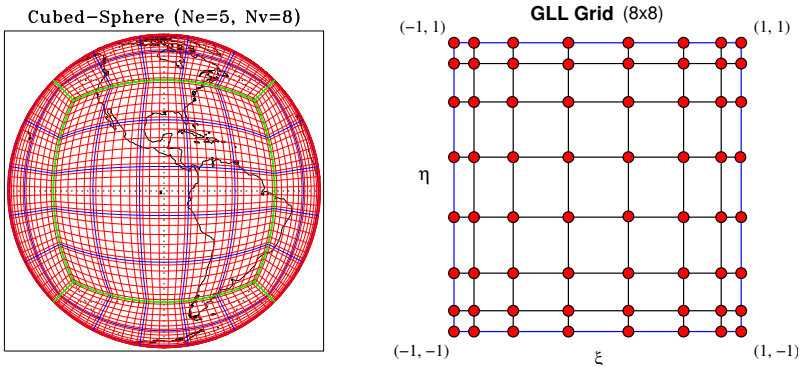

Figure 3: *Left panel shows a cubed-sphere with 150 elements spanning the surface of the sphere, with* 8×8 *Gauss-Lobatto-Legendre (GLL) grid points. These elements are further mapped onto the reference element* $[-1,1] \otimes [-1,1]$. *Right panel shows a reference element with* 8×8 *GLL points.*

The size of an element Ω_{ij} is determined by $\Delta x_i^1 = (x_{i+1/2}^1 - x_{i-1/2}^1)$ and $\Delta x_j^2 = (x_{j+1/2}^2 - x_{j-1/2}^2)$ in the x^1 and x^2-directions, respectively. For $t > 0$, consider an element Ω_{ij} in the partition of Ω and an approximate solution $U_h = U_h(x^1, x^2, t)$ belongs to the finite dimensional space $\mathcal{V}_h(\Omega)$. Multiplication of (13) by a test function $\varphi_h = \varphi_h(x^1, x^2) \in \mathcal{V}_h$ and integration over the element Ω_{ij} results in a weak Galerkin formulation of the problem.

$$\frac{\partial}{\partial t} \int_{\Omega_{ij}} U_h \, \varphi_h \, d\Omega - \int_{\Omega_{ij}} \mathbf{F}(U_h) \cdot \nabla \varphi_h \, d\Omega + \int_{\partial\Omega_{ij}} \mathbf{F}(U_h) \cdot \mathbf{n} \, \varphi_h \, ds = \int_{\Omega_{ij}} S(U_h) \, \varphi_h \, d\Omega, \tag{14}$$

where $\mathbf{n}$ is the outward-facing unit normal vector on the element boundary $\partial\Omega_{ij}$.

Along the boundaries of an element (internal interfaces) $\partial\Omega_{ij}$, the function U_h is discontinuous and the boundary integral (third term in (14)) is not uniquely defined. Therefore, the analytic flux $\mathbf{F}(U_h) \cdot \mathbf{n}$ in (14) must be replaced by a numerical flux $\widehat{F}(U_h^-, U_h^+)$. The numerical flux resolves the discontinuity along the element edges and provides the only mechanism by which adjacent elements interact. For simplicity, the Lax-Friedrichs numerical flux as considered in (3; 22) is chosen for the present study, given by

$$\widehat{F}(U_h^-, U_h^+) = \frac{1}{2} \left[(\mathbf{F}(U_h^-) + \mathbf{F}(U_h^+)) \cdot \mathbf{n} - \alpha (U_h^+ - U_h^-) \right],$$

where U_h^- and U_h^+ are the left and right limits of the discontinuous function U_h evaluated at the element interface, α is the upper bound for the absolute value of eigenvalues of the flux Jacobian $\mathbf{F}'(U)$ in the direction $\mathbf{n}$. Because of the Lagrangian discretization in the vertical direction the 3D baroclinic system may be considered as as vertically stacked shallow water systems, and for which the local maximum values of α in x^1 and x^2-directions for each element Ω_{ij} are defined as in (22), $\alpha^1 = \max\left(|u^1| + \sqrt{\Phi \, G^{11}}\right)$, $\alpha^2 = \max\left(|u^2| + \sqrt{\Phi \, G^{22}}\right)$. Treatment of flux terms and vector quantities at the cube-face edges needs special attention, and it is discussed in (21).

1.4 Space discretization

For each element Ω_{ij}, define the local variables $\xi^k = 2(x^k - x_i^k)/\Delta x_i^k$, with $x_i^k = (x_{i+1/2}^k + x_{i-1/2}^k)/2$ and $k = 1, 2$, denote the x^1, x^2-directions, respectively. By using these relations, an element Ω_{ij} is mapped onto the reference element $\widetilde{\Omega}_{ij} \equiv [-1,1] \otimes [-1,1]$. An important aspect of the DG discretization is the choice of an appropriate set of basis functions (polynomials) that span $\mathcal{V}_h$. While (21; 22) used a modal expansion basis, a high-order nodal basis set is found to be more computationally efficient and used for DG version in HOMME (6; 15). Nodal basis set are popularly used in SE methods (7).

The nodal basis set is constructed using Lagrange-Legendre polynomials $h_\ell(\xi)$, $\xi \in [-1,1]$, with roots at Gauss-Lobatto quadrature points. The basis functions are defined by

$$h_\ell(\xi) = \frac{(\xi-1)(\xi+1)\,L'_N(\xi)}{N(N+1)\,L_N(\xi_\ell)\,(\xi-\xi_\ell)} \tag{15}$$

where $L_N(\xi)$ is the Legendre polynomial of degree N. In the two-dimensional (2D) (ξ^1,ξ^2) coordinate system, the test function (φ_h) as well as the the approximate solution U_h are expanded in terms tensor-product functions from the basis set. Thus,

$$U_h(\xi^1,\xi^2) = \sum_{\ell=0}^{N}\sum_{m=0}^{N} U_{\ell m}\, h_\ell(\xi^1)\, h_m(\xi^2), \quad \text{for} \quad -1 \le \xi^1,\xi^2 \le 1$$

1.5 Time discretization

The above ODE can be solved with a variety of numerical integrators. Strong-stability preserving (SSP) time discretization methods were developed for the semi-discrete method of lines approximation of hyperbolic PDEs in conservative form, Gottlieb et al. (9). Strong stability is resulting from the total variation diminishing property for the internal stages. A 3-stage SSP Runge-Kutta method is given by

$$\begin{aligned} U^{(1)} &= U^n + \Delta t\, L(U^n) \\ U^{(2)} &= \frac{3}{4}U^n + \frac{1}{4}U^{(1)} + \frac{1}{4}\Delta t\, L(U^{(1)}) \\ U^{n+1} &= \frac{1}{3}U^n + \frac{2}{3}U^{(2)} + \frac{2}{3}\Delta t\, L(U^{(2)}). \end{aligned}$$

To compute $U_h^{(k)}$ for each stage requires up to 3 evaluations of the right-hand side $L(U_h^{(k)})$. Thus, Because of rhs evaluations per stage, higher-order SSP Runge-Kutta methods can be expensive, in terms of the number of floating point operations, memory to store intermediate stages and communication overhead per time step. This is the default time integration for DG dynamical core in HOMME.

HOMME employs the Boyd-Vandeevan type filter and in addition to that a ∇^2 diffusion is applied to the momentum equations, in the DG formulation.

2 Preliminary Results with Baroclinic DG model

2.1 Baroclinic instability test

The DG conservative dynamical core is evaluated using a baroclinic test suggested by Jablonowski and Williamson (12). This test asses the evolution of an idealized baroclinic wave in the Northern hemisphere. The initial conditions are quasi-realistic and defined by analytic expressions, and the test design guarantees static, inertial and symmetric stability properties, but unstable with baroclinic instability mechanism. The balanced initial flow field comprises a zonally symmetric state with a jet in the mid-latitueds of each hemisphere and a quasi-realistic temperature distribution as shown in Fig. 4.

Figure (5) shows the surface pressure (P_s) after 6 and 10 days (left and central panels), and temperature field at 850 hPa after 10 days (right panel) of model integration. For this simulation the model uses an *average* horizontal resolution of 1.7° approximately, and other grid configurations are $N_e = 6$ (or total 216 elements) with 10×10 GLL points, and 26 vertical levels. The evolution of baroclinic waves is nicely captured in the model simulation, and the results compare favorably to the reference results given in (12).

The DG baroclinic model 8 days simulation is compared with that of the NCAR T42 global spectral model. Here DG model uses an *average* resolution of 2° along the equator. As compared to the DG baroclinic model simulation captures baroclinic disturbance (both pressure variation and temperature fields) very well and pressure fields seems to be less oscillatory than T42 case as shown in Fig. 6. Figure 7 shows

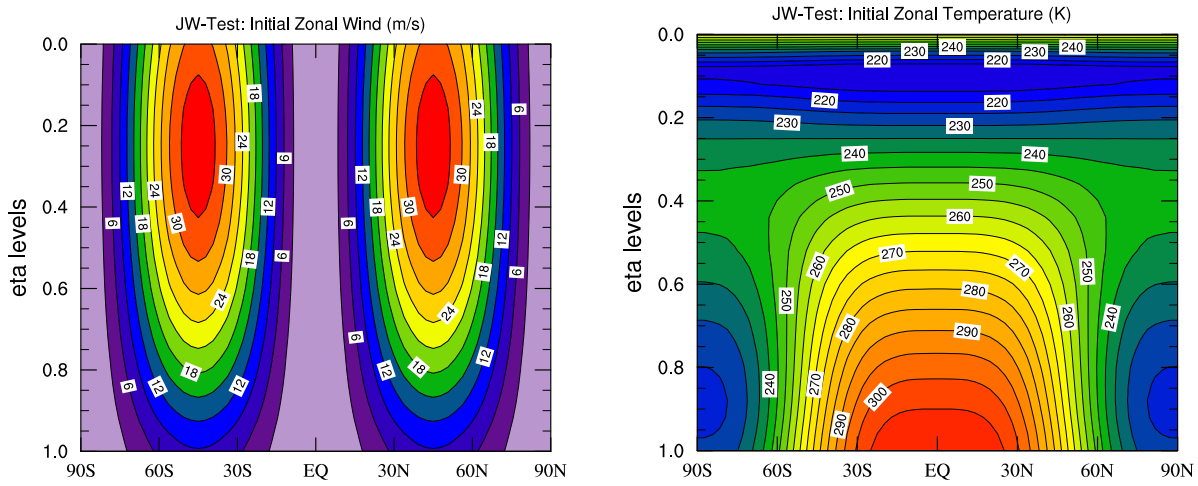

Figure 4: *The initial conditions for the unperturbed zonal wind u (left) and the temperature filed T (right). The initial conditions are quasi-realistic and defined by analytic expressions (12).*

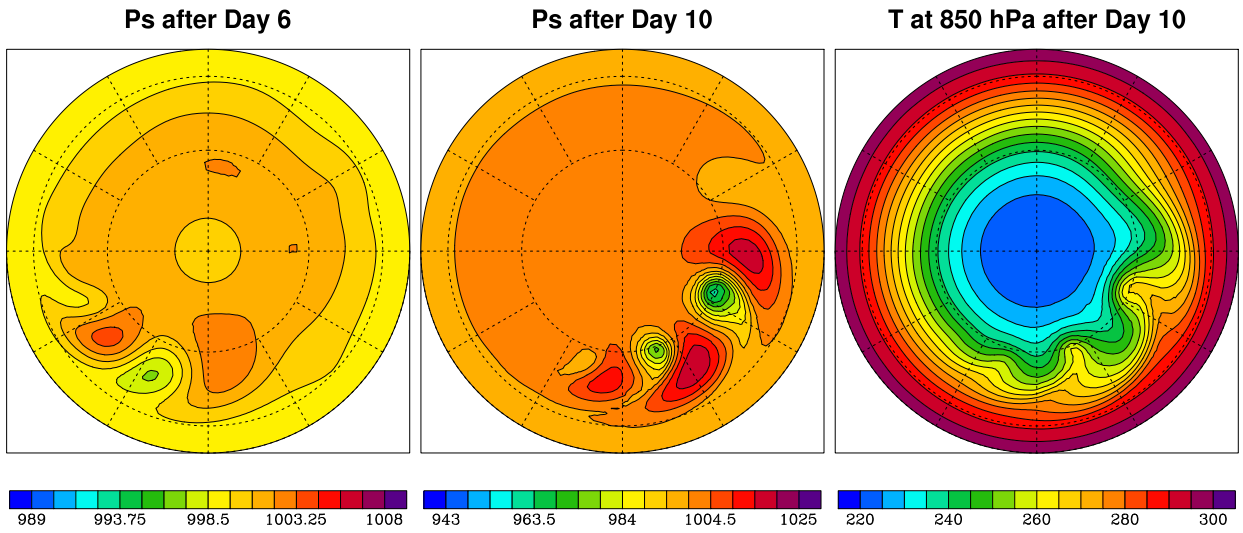

Figure 5: *Jablonowski-Williamson baroclinic instability test (12) with the DG dynamical core. The left and central panels show the surface pressure after 6 and 10 days of model integration, respectively. The right panel shows temperature field at 850 hPa after 10 days of integration. The DG model with 216 spectral elements, each with* 10×10 *GLL points, and 26 vertical levels used for this simulation.*

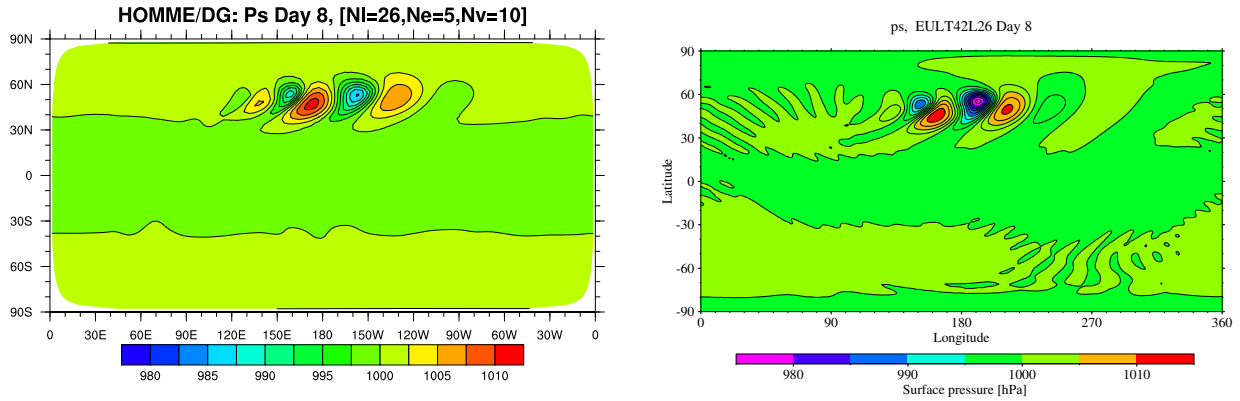

Figure 6: *The surface pressure after 8 days of model simulation for the DG model (left) and the corresponding reference surface pressure with NCAR T42 simulation (right).*

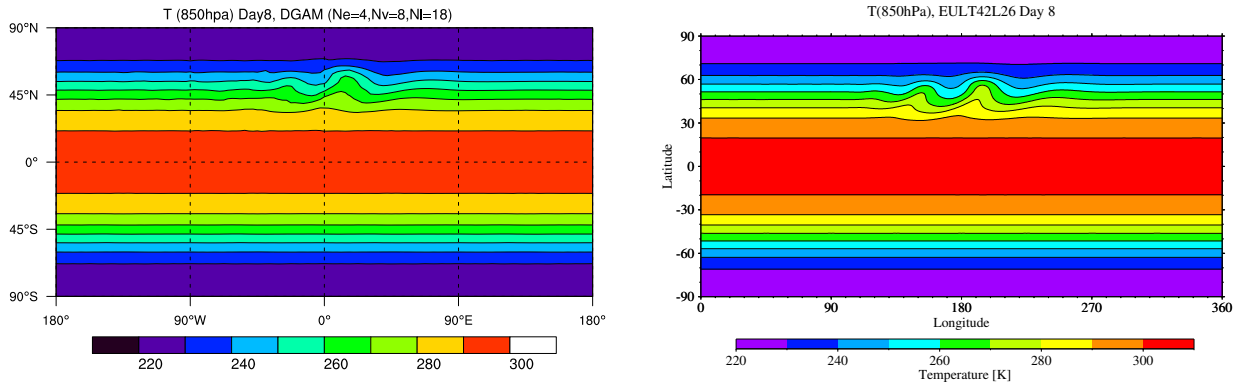

Figure 7: *The Temperature field at 850 hPa for the DG model after 8 days of model simulation (left) corrsponding temperature with NCAR T42 model (right). A low resolution version of the DG model is used for this test ($Nl = 18$, $Ne = 4$, $Nv = 8$).*

the temperature filed at 850 hPa after 8 days of the simulation with a low-resolution DG run against T42 run. The grid convergence of the numerical solution for the baroclinic test is done with varying number of element resolution as shown in Fig. 8. More rigorous quantitative comparison of DG baroclinic model with different models (12) will be reported in (19).

2.2 Preliminary scaling results with baroclinic model

Strong scaling results with $N_e = 12$ (i.e., total 864 elements) and for baroclinic instability (12) simulations are shown in Performance data is obtained on an IBM Blue Gene/L supercomputer with 2048 CPUs capable of 5.73 TFLOPS peak (2). Sustained performance of 194 to 222 Mflops per second per processor (8% peak) are attained in coprocessor mode and 178 to 209 Mflops per second per processor (8% peak) in virtual-node mode. Note that the model is still under development and expect that the final product will exhibit levels of single processor performance and scalability comparable to those exhibited by the spectral element dynamical core in HOMME

Many desirable options, such as monotonic filter for the DG transport, will be added in the near future. The model has options for divergence damping and explicit diffusion. Moreover, a conservating remapping scheme with monotonic option has been developed to interpolate data between cubed-sphere and regular latitude-logitude grids (14). This scheme will act as a coupler between the DG dynamical core and standard physics package such as CAM based on latitude-logitude spherical grids.

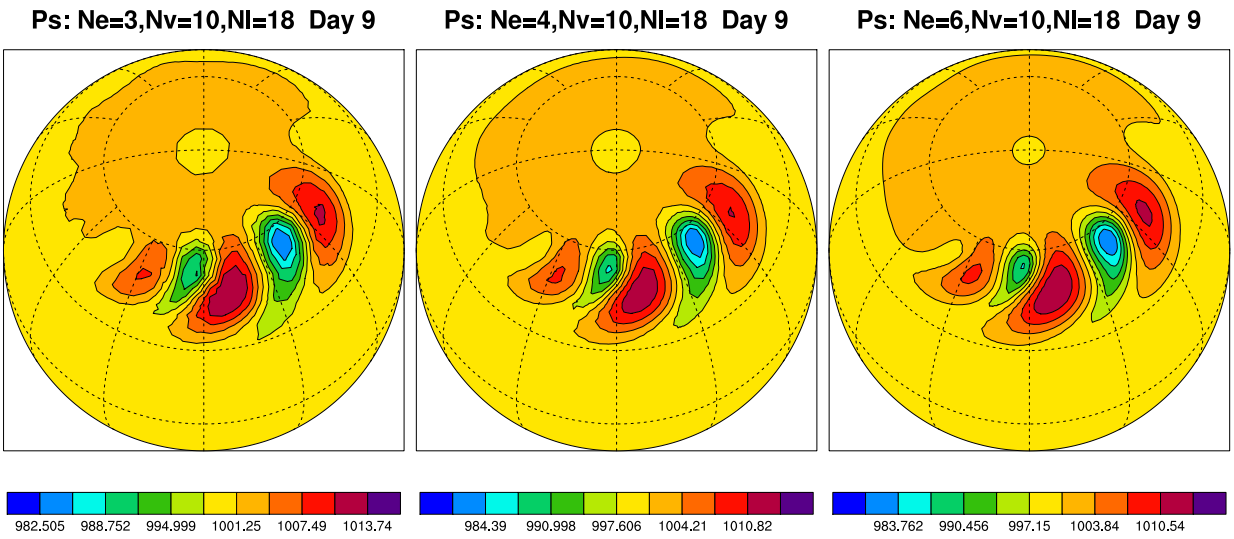

Figure 8: *Convergence of solution (surface pressure) with varying number of element resolution*

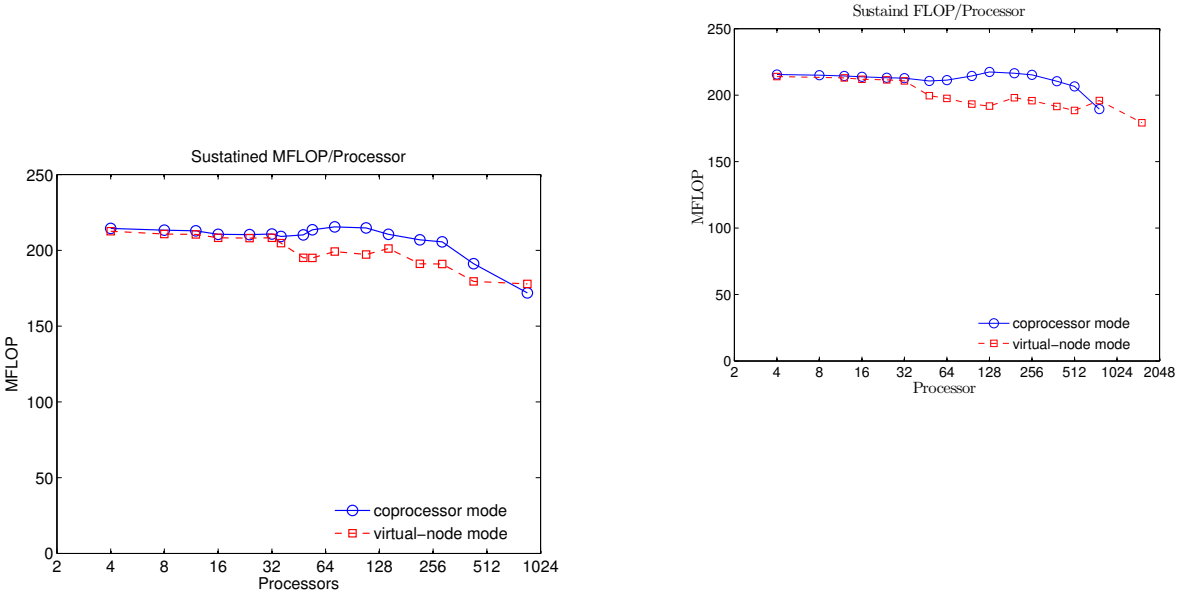

Figure 9: *Preliminary scaling results (sustained Mflops) with DG model for the baroclinic instability test on IBM BG/L (1024 DP nodes, 700 MHz PPC 440s). Parallel performance (strong scaling) results for* $Ne = 12$ *(left) and* $Ne = 16$ *(right).*

2.3 Long-term integrations

A variety of standard benchmark calculations for long term integrations have been proposed as a means of evaluating primitive equations. In the HOMME framework the available options are dry and moist Held-Suarez (10) and aqua-planet simulations. In the Held-Suarez test case the thermal structure of the model atmosphere is relaxed to a prescribed radiative-convective equilibrium. This test emphasizes the simplified forcing to the momentum and thermodynamic equations. A low-resolution of the DG baroclinic model with 26 vertical levels and 216 elements ($N_e = 6$, $N_v = 6$) are used for the simulations. A *moderate* diffusion ($\nu = 1.0 \times 10^5$) used for the 1200-day simulations and the average values of zonal mean wind and temperature fields are computed for the last 1000 days. The vertical structure of the wind and temperature field are well captured in the simulation, however, surface temperature and the zonal jets appeared to be more stronger in the preliminary simulation than the reference solution. This experiment is sensitive to the diffusion coefficient, and its optimal choice in terms of accuracy with the reference solution is the part of ongoing research effort and will be reported in (19). We also plan to perform long-term integrations such as the moist Held-Suarez and aqua-planet tests. However, this experiments requires a monotonic (non-oscillatory) transport scheme consistent with the high-order dynamics.

3 Monotonic scheme for scalar advection

In theory the large scale atmospheric flows do not contain severe shocks and discontinuities, therefore the 'system limiting' is not necessary to control spurious oscillations in the flow field. However, there are quantities such as moisture variables and chemical mixing rations which need to be monotonic (positivity preserving) during the atmospheric transport process. Modeling monotonic (non-oscillatory) and conservative transport processes by using a high-order numerical method is remain to be a big challenge. A variety of slope limiters exist for relatively low-order ($N \leq 3$) DG schemes and unfortunately, none of the existing limiters are found to be satisfactory for directly applying in high-order DG methods. The limiting methods used for DG schemes are based on classical finite-volume methods and employ the element *average* values rather than the available high-order element grid point values in the limiting or reconstruction processes.

A basic problem with such limiters is that when the element size becomes larger (i.e., number of GLL points increases) the monotonic element based limiting leads to poorly resolved low quality solutions as demonstrated in (13). Spectral Finite-Volume (SFV) method (**?**) is a new approach in high-order (conservative) methods, which has the nice feature of intra-element flux operations (limiting). Recently we have developed a nodal SFV advection scheme (1) which couples flux corrected transport algorithm (FCT) to control spurious oscillations. However, as compared to the DG methods, SFV/FCT scheme is more computationally expensive due to the reconstruction process in each control volumes within an element. Figure 10 shows preliminary results with SFV advection test (solid-body rotation), where the FCT filter clearly removes the spurious oscillations.

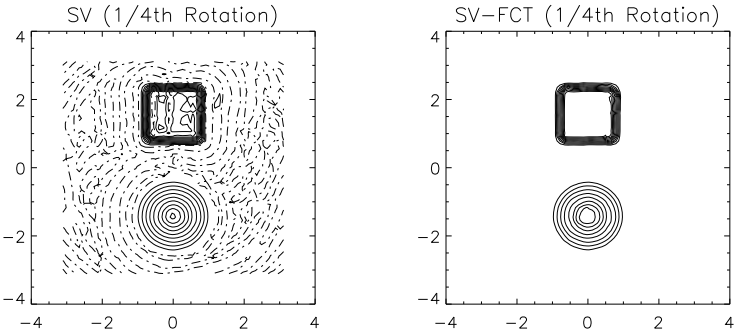

Figure 10: *The spectral finite volume (SFV) solution for the advection problem. Left panel shows solution without any filter and right panle show SFV-FCT combined solution*

The WENO based limiters (24) are becoming popular in DG methods. However, for the high-order applications these limiters are not only computationally expensive but for limiting a particular element the scheme requires a large halo region made of surrounding elements. For practical implementation the WENO based high-order limiters ($N > 3$) can be a potential parallel-communication bottleneck, particularly for the HOMME framework where higher-order ($N \geq 6$) spectral elements are typically used.

In order to have a *practical* limiter, we combine theses low-order limiting operations in the HOMME/DG framework. We have developed a new monotonic limiting procedure for high-order DG advection schemes which has the capability of intra-element limiting. The idea is similar to that used in SFV methods where a rectangular spectral element is partitioned into sub-elements (control volumes) and then the low-order DG limiter is applied to each of the sub-elements. The limited solution can be remapped back into the original grid. The partition of the elements can be done in a conservative manner such that it is consistent with total degrees of the freedom within an element. A low-order DG-WENO scheme or a minmod limiter may be used for sub-element limiting, which has excellent properties to control spurious oscillations for non-smooth flows (24; 15). Figure 11 shows analytic and a third-order DG-WENO solution for highly deforming and non-smooth test problem (Doswell votex) considered in (1; 15). Note that the this method do not degenerate the entire model to a low-order method, it only affects the advecting scalar fields. This limiter will be used for long-term integrations such as the moist Hels-Suarez and aqua-planet simulations in HOMME.

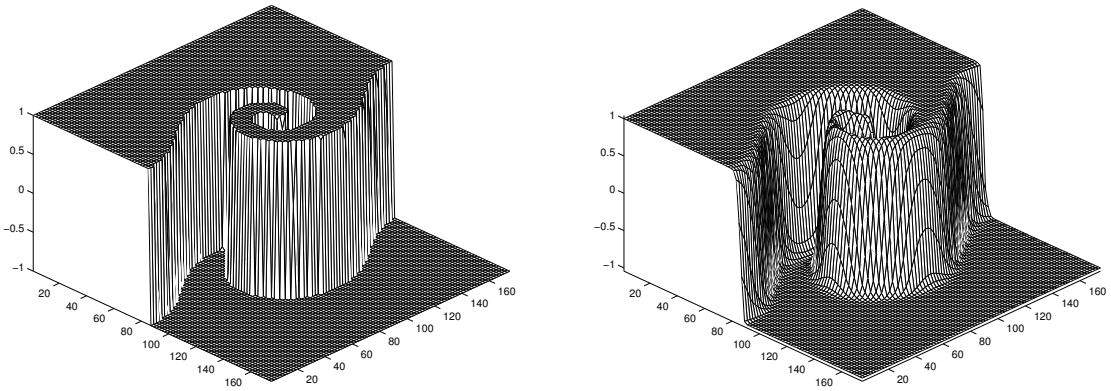

Figure 11: *Analytic solution (left panel) and numerical solution (right panel) for a non-smooth defomational flow problem (15). The numerical solution is produced by a DG scheme combined with the WENO limiter.*

Climate Simulation with the Isentropic Finite Volume Dynamical Core of the Community Atmosphere Model

Chih-Chieh (Jack) Chen, Philip R. Rasch and Henry M. Tufo
National Center for Atmospheric Research
Boulder, CO 80307-3000

Part of our proposal focuses on producing an accurate representation for processes involving the vertical coordinate in atmospheric models.

To this end we have been exploring the use of quasi-isentropic vertical coordinates in atmospheric models. We have begun this exploration in the context of the finite volume (FV) dynamical core of the Community Atmosphere Model (CAM) with the plan to map what we have learned to the HOMME computational environment as the effort matures.

One of the innovations in the FV dynamical core is the introduction of a Lagrangian coordinate in the vertical (see (36)). In the FV dynamical core, model variables are periodically remapped to a prescribed vertical coordinate and this procedure, so-called vertical remapping, accounts for vertical transport induced by the atmospheric motions. (37) demonstrated that the FV dynamical core represented atmospheric transport in the most realistic way of the three dynamical cores in CAM. Nevertheless, some undesirable vertical

transport could still be produced due to the choice of a vertical coordinate. Currently, the FV core remaps to a pressure based vertical coordinate, and the consequence is that non-physical vertical transport may be introduced. To eliminate such undesirable transport, an isentrope-based vertical coordinate was developed to improve the accuracy of the atmospheric transport in the FV dynamical core.

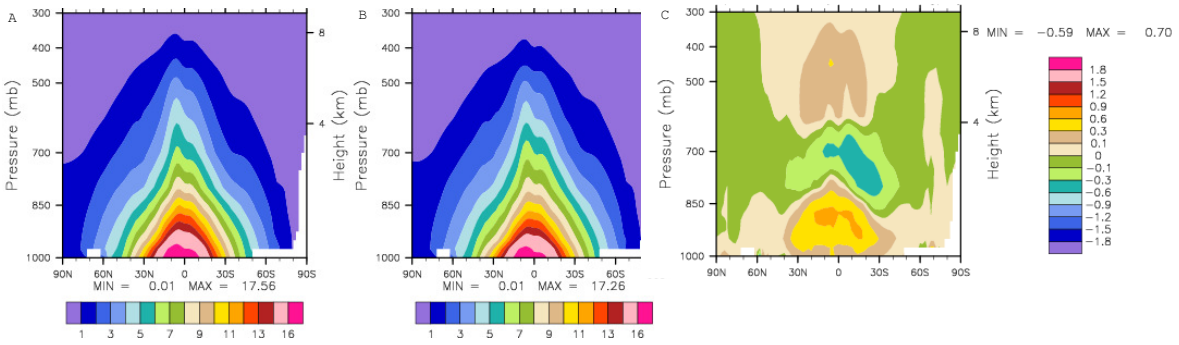

Figure 12: Annual mean of zonally-averaged specific humidity (g/kg): (a) simulation by the isentropic FV model, (b) simulation by the default FV model, and (c) difference between (a) and (b).

We have formulated a hybrid isentropic coordinate following the formulation described in (38), and a 10-year climate simulation has been performed using the isentropic model. The isentropic model has made significant improvements over that of the current CAM in the simulated climatology. As shown in Fig. 12, water vapor is more strongly confined in the lower troposphere in the isentropic model when compared with the default η model, implying vertical transport has been suppressed. The equatorial lower troposphere becomes more moist and the mid-troposphere has become drier (Fig. 12c). This is reflected with the cloud distribution, as shown in Fig. 13: more low clouds are present in the equatorial lower troposphere within the isentropic model. Furthermore, the high-level cloud is significantly reduced and this is more consistent with observation.

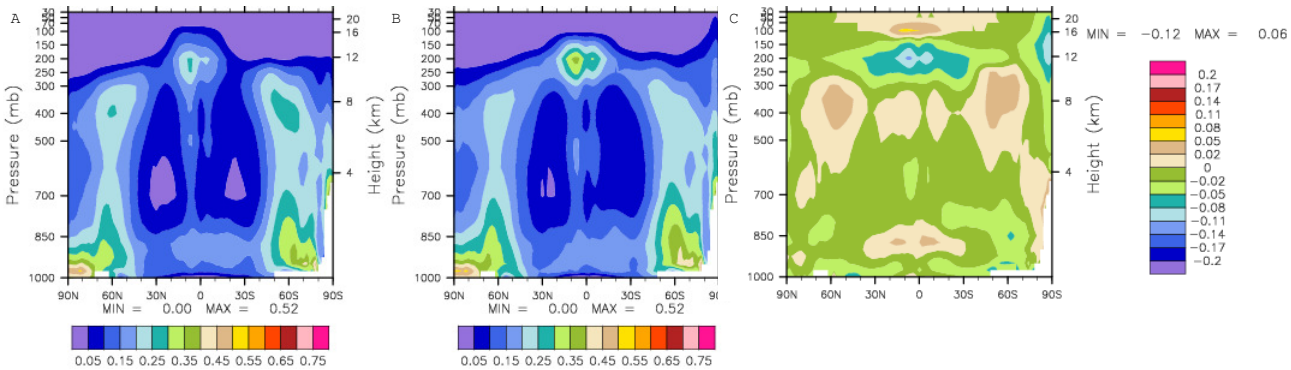

Figure 13: Annual mean of zonally-averaged cloud fraction: (a) simulation by the isentropic FV model, (b) simulation by the default FV model, and (c) difference between (a) and (b).

While the reduction of high clouds in the isentropic model may result from the very different characteristics of atmospheric transport (vertical transport of water vapor), another factor may play an even bigger role. (35) found that most general circulation models tend to produce an atmospheric state up to 10° C too cold and he interpreted such general cold biases through the second law of thermodynamics. He also argued that an isentropic coordinate system may remedy this problem. As seen in Fig. 14, the default FV model does possess the cold bias phenomenon as described in (35), most pronounced in the summer polar upper troposphere and stratosphere. This cold feature is also present in 22 of the 23 models that participated in the soon to be released fourth assessment of the Intergovernmental Panel on Climate Change, and has been a persistent feature in GCMs for 20 years. As demonstrated in Fig. 15c and f, the isentropic model produces

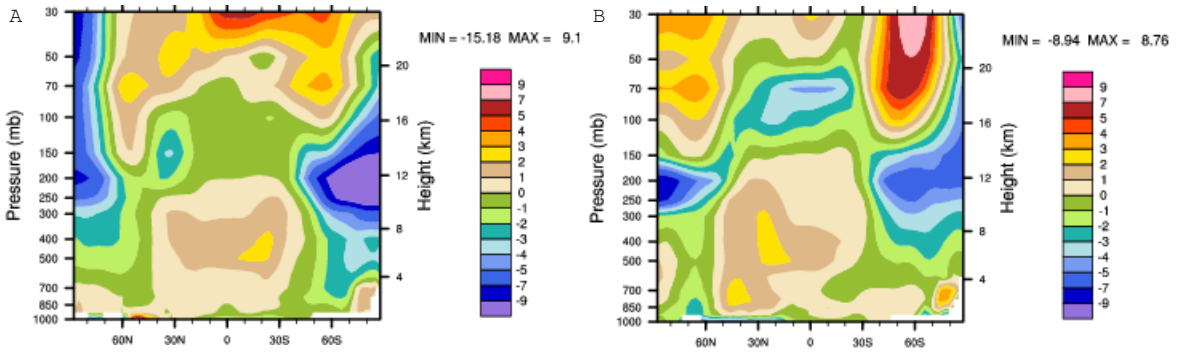

Figure 14: Difference in the zonally-averaged temperature field between the default FV model and ECMWF reanalysis: (a) DJF and (b) JJA.

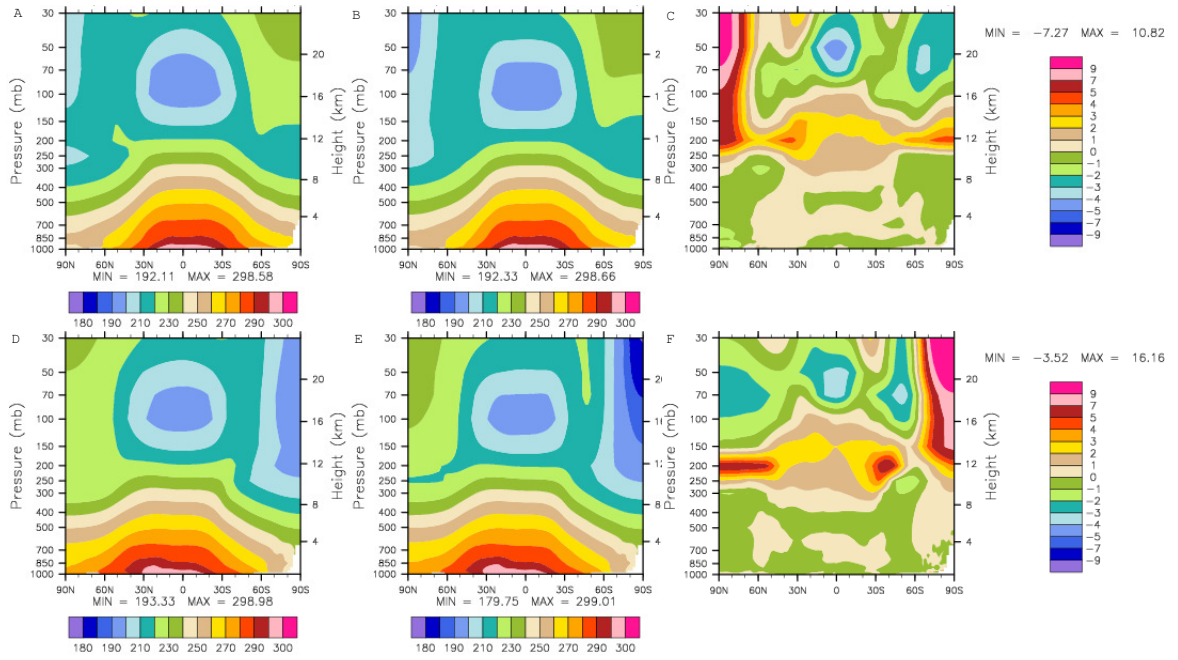

Figure 15: Zonally-averaged temperature and difference: (a) simulation by the isentropic FV model in DJF, (b) simulation by the default FV model in DJF, (c) difference between (a) and (b), (d) simulation by the isentropic FV model in JJA, (e) simulation by the default FV model in JJA, (f) difference between (d) and (f)

significant warmer upper troposphere and stratosphere, most noticeable in the polar upper atmosphere. The equatorial upper troposphere is also warmer and it leads to a reduction in relative humidity. The high-level cloud (which is a function of relative humidity) thus significantly decreased (compare Fig. 15 and Fig. 13).

Another bias observed in the climate simulation (in CAM, and many other GCMs) is the sea-level pressure in the Northern Hemisphere during the winter months. When compared with the NCEP reanalysis, the default FV model tends to produce much stronger lows near the North Atlantic and under-estimate the strength of the Aleutian Low (compare Fig. 16b and Fig. 16c). This has a significant impact on the surface wind field which drives the ocean circulation in these regions. In the isentropic model, such bias is highly reduced and the sea-level pressure distribution is closer to observation (Fig. 16a).

We have explored many other aspects of the change in vertical coordinate and remapping algorithms that are not described above. In addition to the changes in circulation and climate features discussed here, there

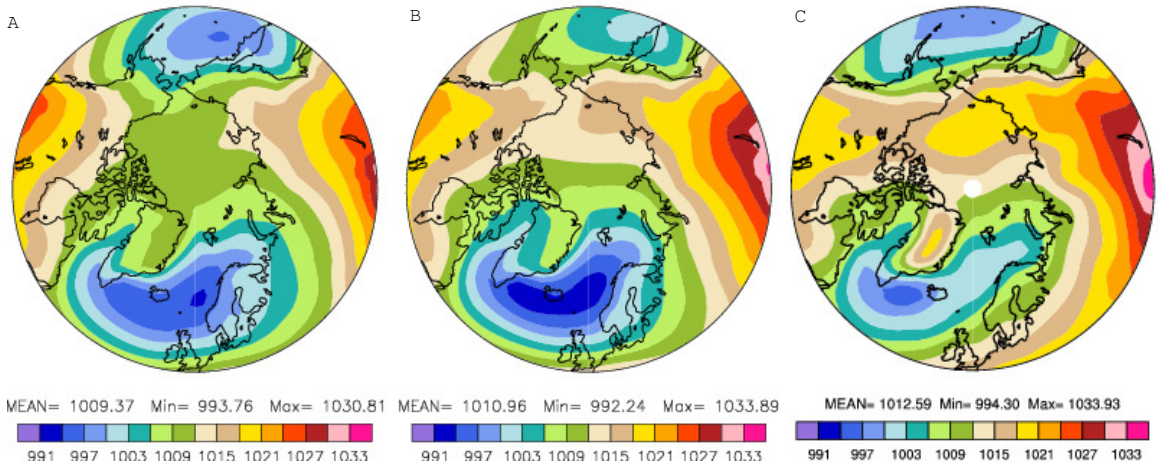

Figure 16: Sea-level pressure in the Northern Hemisphere in DJF: (a) simulation by the isentropic FV model, (b) simulation by the default FV model, and (c) NCEP reanalysis.

are also important changes to the simulation and transport of trace constituents.

Some of these results have been presented at the Xth annual meeting on PDEs on the Sphere (Monterrey, CA, June 2006), and at the December AGU in San Francisco. Manuscripts are now being prepared for submission to peer reviewed journals.

References

[1] Cheruvu V., R. D. Nair, and H. M. Tufo, 2007: A spectral finite volume transport scheme on the cubed-sphere. *Applied Num., Math.*, In press.

[2] Choi H-W., R. D. Nair, and H. M. Tufo, 2006: A scalable high-order discontinuous Galerkin method for global atmospheric modeling. Proceedings of the *Parallel CFD 2006*, May 15-18, Busan, South Korea.

[3] Cockburn, B., G. E. Karniadakis, and C. W. Shu, 2000: Discontinuous Galerkin Methods. *Springer-Verlag*, New York, 470 pp.

[4] Dennis, J. M., 2003: Partitioning with Space-Filling Curves on the Cubed-Sphere. Proceedings of Workshop on Massively Parallel Processing IPDPS'03 Nice, France, April 2003.

[5] Dennis, J.M., R.D. Nair, H.M. Tufo, M. Levy, and T. Voran, 2006: Development of a Scalable Global Discontinuous Galerkin Atmospheric Model. *Int. J. of Comput. Sci. Eng.*, in press.

[6] Dennis, J.M., A. Fournier, W. Spotz, A. St.-Cyr, M. Taylor, S.J. Thomas, and H.M. Tufo., 2005: High Resolution Mesh Convergence Properties and Parallel Efficiency of a Spectral Element Atmospheric Dynamical Core. *Int. J. of High Perf. Comput. App.*, **19**, 225–235.

[7] Deville, M. O., P. F. Fischer, and E. H. Mund, 2002: High-Order Methods for Incompressible Fluid Flow. *Cambridge University Press*, 499 pp.

[8] Emanuel, K., and Zivkovic-Rothman, M., 1999: Development and evaluation of a convection scheme for use in climate models. *J. Atmos. Sci.*, **56**, 1766–1782.

[9] Gottlieb, S., C. W. Shu, and E. Tadmor, 2001: Strong stability preserving high-order time discretization methods. *SIAM Review*, **43**, 89–112.

[10] Held, I. H., M. J. Suarez 1994: A proposal for the intercomparison of the dynamical cores of atmospheric general circulation models, *Bull. Amer. Meteor. Soc.*, **75**, 1825-1830

[11] HOMME: High-Order Methods Modeling Environment, 2006: `http://www.homme.ucar.edu/`

[12] Jablonowski, C.J., and D.L. Williamson, 2006: A baroclinic wave test case for dynamical cores of general circulation models: model intercomparisons. *NCAR/TN-469+STR.*

[13] Iskandrani, M., J. Levin, B. Choi and D. Haidvogel, 2005: Advetion scheme for high-order *h-p* finite element and finite volume methods. *Ocean Modeling*, **10**, 233-252.

[14] Lauritzen, P. H., and R. D. Nair, 2007: High-order monotonic and conservative remapping between spherical grids: Regular latitude-longitude grid and cubed-sphere geometry. submitted to Mon. Wea. Rev.

[15] Levy, M. N., R. D. Nair, and H. M. Tufo, 2007: High-order Galerkin method for scalable global atmospheric models. *Computers and Geosciences*, In press.

[16] Lin, S-J., 2004: A vertically Lagrangian finite-volume dynamical core for global models. *Mon. Wea. Rev.*, **132**, 2293–2307.

[17] Loft, R. et al., 2005: Establishing a Petascale Collaboratory for the Geosciences: Technical and Budgetary Prospectus. Report of the Technical Working Group and Ad Hoc Committee for a Petascale Collaboratory for the Geosciences, National Science Foundation, June. `http://www.joss.ucar.edu/joss_psg/meetings/petascale/petascale_tech_10.20.05.pdf/.`

[18] Loft, R. D., Thomas, S. J. and Dennis, J. M. (2001) Terascale spectral element dynamical core for atmospheric general circulation models Supercomputing 2001, ACM/IEEE conference, November 2001, Denver.

[19] Nair, R. D., H. W. Choi, and H. M. Tufo, 2007: A high-order conservative dynamical core for climate modeling. In prepartion, to be submitted to *Mon. Wea. Rev.*

[20] Nair, R. D. and H. M. Tufo, 2006: A scalable High-Order Dynamical Core for Climate Modeling. Proceedings of International Conference on Mesoscale Process in Atmosphere, Ocean and Environment Systems. IMPA 2006, Feb. 14th-17th, IITD, New Delhi, India.

[21] Nair, R. D., S. J. Thomas, and R. D. Loft, 2005: A discontinuous Galerkin transport scheme on the cubed-sphere. *Mon. Wea. Rev.*, **133**, 814–828.

[22] Nair, R. D., S. J. Thomas, and R. D. Loft, 2005: A discontinuous Galerkin global shallow water model. *Mon. Wea. Rev.*, **133**, 876–888.

[23] Nair, R. D. and B. Machenhauer, 2002: The mass conservative cell-integrated semi-Lagrangian scheme on the sphere. *Mon. Wea. Rev.*, **130**, 649–667.

[24] Qui, J., and C.-W. Shu, 2005: Runge-Kutta discontinuous Galerkin method using WENO limiters. *SIAM J. Sci. Comput.*, **26**, 907-929.

[25] Rancic, M., R. J. Purser, and F. Mesinger, 1996: A global shallow-water model using an expanded spherical cube: Gnomic versus conformal coordinates. *Q. J. R. Meteorol. Soc.*, **122**, 959–982.

[26] Sadourny, R., 1972: Conservative finite-difference approximations of the primitive equations on quasi-uniform spherical grids. *Mon. Wea. Rev.*, **100**, 136–144.

[27] Sagan, H. 1994: *Space-Filling Curves* Springer-Verlag, 1994.

[28] Sawyer, W. B., and A. A. Mirin 2004: A Scalable Implementation of a Finite-Volume Dynamical Core in the Community Atmosphere Model, In Proceedings of Parallel and Distributed Computing and Systems 2004.

[29] Starr, V. P., 1945: A quasi-Lagrangian system of hydrodynamical equations. *J. of Meteorology*, **2**, 227–237.

[30] St-Cyr, A., J.M. Dennis, R. Loft, S.J. Thomas, H.M. Tufo, and T. Voran, 2006: Early Experiences with the 360TF IBM BlueGene/L Platform. *Int. J. of Comput. Meth.*, accepted.

[31] St-Cyr, A., M.J. Gander, and S.J. Thomas 2005: Optimized restricted additive Schwarz. *Lecture Notes in Computational Science and Engineering*, Springer Verlag.

[32] Thomas, S. J., and R.D. Loft, 2000: Parallel semi-implicit spectral element methods for atmospheric general circulation models. Journal of Scientific Computing **15**, 499–518.

[33] Thomas, S.J., and R.D. Loft, 2002: Semi-implicit spectral element atmosphere model. Journal of Scientific Computing **17**, 339–350.

[34] Thomas, S. J., and R.D. Loft, 2005: The NCAR spectral element climate dynamical core: Semi-implicit Eulerian formulation. J. Sci. Comput. **25**, 307–322.

[35] Johnson, D. R., 1997: "General coldness of climate models" amd the second law: Implications for modeling the earth system. *J. Climate*, **10**, 2826–2846.

[36] Lin, S.-J., 2004: A "vertically Lagrangian" finite volume dynamical core for global models. *Mon. Wea. Rev.*, **132**, 2293–2307.

[37] Rasch, P. J., D. B. Coleman, N. Mahowald, D. Williamson, S.-J. Lin, B. A. Boville and P. Hess, 2006: Characteristics of atmospheric transport using three numerical formulations for atmospheric dynamics in a single GCM framework. *J. Climate*, **19**, 2243–2266.

[38] Schaack, T. K., T. H. Zapotocny, A. J. Lenzen and D. R. Johnson, 2004: Global climate simulation with the University of Wisconsin global hybrid isentropic model. *J. Climate*, **17**, 2998–3016.